Modeling high temperature deformation characteristics of AA7020 aluminum alloy using substructure-based constitutive equations and mesh-free approximation method

Eivani, A. R.; Vafaeenezhad, H.; Nikan, O.; Zhou, J.

DOI
10.1016/j.mechmat.2018.11.011

Publication date
2019

Document Version
Accepted author manuscript

Published in
Mechanics of Materials

Citation (APA)
Eivani, A. R., Vafaeenezhad, H., Nikan, O., & Zhou, J. (2019). Modeling high temperature deformation characteristics of AA7020 aluminum alloy using substructure-based constitutive equations and mesh-free approximation method. *Mechanics of Materials*, *129*, 104-112. https://doi.org/10.1016/j.mechmat.2018.11.011

Modeling high temperature deformation characteristics of AA7020 aluminum alloy using substructure-based constitutive equations and mesh-free approximation method

A. R. Eivani [1], H. Vafaeenezhad [1, ∗], O. Nikan [2], J. Zhou [3]

[1] *School of Metallurgy and Materials Engineering, Iran University of Science and Technology (IUST), Narmak, Tehran, Iran.*

[2] *School of Mathematics, Iran University of Science and Technology (IUST), Narmak, Tehran, Iran.*

[3] *Department of Biomechanical Engineering, Delft University of Technology, Mekelweg 2, 2628 CD Delft, The Netherlands*

Abstract

This research was aimed to assess the potential of a radial basis function (RBF) approximation method against the dislocation substructure-based constitutive model in predicting high-temperature deformation behavior of the AA7020 aluminum alloy. Hot compression tests were performed over a range of strain rate of 0.1-100 s^{-1} and a range of temperature of 350-500 ^{o}C up to a strain of 0.6. The hot deformation behavior of the alloy was first described by a substructure kinetic-based constitutive equation, with the effects of strain, strain rate and temperature together with dynamic recovery parameters taken into consideration. A RBF approximation method was then developed to model the flow behavior of the material. The RBF model, as a kind of novel mesh-free function estimation approach, was trained and tested with the obtained datasets from the hot compression tests. The performance of the developed analytical and neural computational models was evaluated using

---

∗ Corresponding author, Tel: +982177240540, Fax: +982177240480
E-mail address: hossein.vafa@gmail.com (H.Vafaeenezhad)

statistical criteria. The results showed that the RBF model was more proficient and accurate in predicting the hot deformation behavior of this aluminum alloy than the substructure-based constitutive model.

Keywords: Radial Basis Function; Hot deformation; Constitutive equation; Aluminum alloy

1 Introduction

7000 series aluminum alloys with Zn and Mg as the major alloying elements possess an excellent combination of strength and fracture toughness, as well as good stress corrosion cracking (SCC) resistance, and are thus extensively used in the aircraft and aerospace industries (Deng et al., 2011; Oliveira et al., 2004). Hot workability of these alloys is affected mainly by their microstructure characteristics that are primarily determined by the Zn/Mg ratio and Cu concentration (Jin et al., 2009). The evolution of microstructural characteristics during hot deformation is governed by the thermomechanical conditions applied and the stacking fault energy (SFE) values of the alloys (Humphreys and Hatherly, 2012). Hence, the studies on the hot deformation behavior and associated microstructural changes at elevated temperatures are of fundamental importance for optimized processing of 7000 series aluminum alloys.

The hot deformation behavior of a particular aluminum alloy is often related to a number of metallurgical phenomena, such as work hardening, dynamic recovery (DRV), dynamic recrystallization (DRX), precipitation hardening, superplasticity and flow instability (Holm et al., 2003; Liu et al., 2010). The relationships between high-temperature flow stress and these metallurgical phenomena are complex and non-linear, which makes reliable prediction of the hot workability of an alloy of interest intricate. A considerable amount of research has recently been performed in this regard and different approaches, such as analytical (Mirzadeh and Parsa, 2014; Shalbafi et al., 2017; Wen et al., 2015), numerical (Haghdadi et al., 2016; Huang and Logé, 2017; Zouari et al., 2016) and artificial intelligence

(Ashtiani and Shahsavari, 2016; Yao et al., 2014; Zhao et al., 2014) models, have been used to predict the hot deformation characteristics of different alloys at elevated temperatures. Although many of these methods are able to yield good results for describing deformability, each of these methods has its own shortcomings. Physically based analytical models, based on the kinetics of dislocation motion and accumulation, for example, need a deep understanding of the plastic deformation mechanisms involved in hot deformation which control the generation and development of the substructure and are affected by the temperature and strain rate applied.

Over the last ten years, meshless methods have attracted a lot of attention in the research community and gained significant importance for providing numerical solutions to various types of engineering problems. Radial basis function (RBF) is an efficient method for approximating or interpolating multidimensional scattered data, since the method is meshless and can be remarkably accurate. RBFs have been applied in other areas in addition to the interpolation of scattered data on subsets of multidimensional space (Fasshauer, 2007). In comparison with the mesh-based methods, such as finite element method (FEM), finite volume method (FVM) and finite difference method (FDM), the meshless methods use a set of random or uniform points which are not interlinked in the form of mesh (Fasshauer, 2007). The RBF methods may be considered as a sort of compromise between FEM and the pseudo-spectral (PS) methods (Buhmann, 2003). The RBF methods are based on expansion into the basis functions that have a spatial location as with FEM. By studying sample data, RBF-based computation can not only preserve high accuracy and be adaptive while facing non-linear data, but also learn data patterns and generalize its learned knowledge (Wendland, 2004).

In the past years, a number of investigations have been carried out to study the hot deformation, related annealing phenomena and microstructural evolution of some typical aluminum alloys. Processing maps of Al alloys have been used to assess the efficiency of power dissipation and metallurgical instability in order to optimize hot working conditions (Lin et al., 2013; Raj, 1981;

Srinivasan et al., 2008; Wang et al., 2015). The kinetics of DRV and DRX of many Al alloys has been investigated as well (Blum et al., 1996; Hausselt and Blum, 1976; Sakai et al., 2009). In addition, some phenomenological and physically based constitutive models have been developed to predict the recrystallization, grain and subgrain growth of these alloys using Monte Carlo simulation (Eivani et al., 2014; Eivani et al., 2012; Radhakrishnan et al., 1998; Shen et al., 2007). A hybrid finite element-cellular automaton method using probabilistic models has been utilized to analyze the static recrystallization (SRX) behavior (Raabe and Becker, 2000; Salehi and Serajzadeh, 2012). Their accuracies depend on the physical assumptions made.

Despite the research to model the hot deformation behavior and microstructural evolution of some Al alloys, dislocation substructure-based constitutive models have not been developed to accurately describe the high-temperature deformation characteristics of aluminum alloys with high SFE values. In the present research, a substructure-based constitutive model and a RBF model were developed to describe and to predict the hot deformation behavior of the AA7020 aluminum alloy. Deformation temperature, strain rate and strain were used as input datasets of the models and the flow stress was assumed to be the output. The predictability of the RBF model was evaluated against the substructure-based constitutive model in terms of relative error R^2 and average root mean square error (RMSE).

2 Experimental procedure

As-extruded AA7020 aluminum alloy was received with a diameter of 48 mm. Table 1 gives the chemical composition of the alloy used. The homogenized ingot was machined to cylindrical specimens with a diameter of 10 mm and a height of 12 mm. Compression tests were carried out using a Gleeble thermomechanical simulator at temperatures of 350, 400, 450 and 500 ^{o}C and strain rates of 0.1, 1, 10, 25, 45 and 100 s^{-1}. The specimens were compressed up to a strain of 0.6 and then quenched in water immediately. Isothermal compression tests were repeated at least twice at each condition. The specimen was heated to a desired deformation temperature at a heating rate of 10 °C/s and held at that temperature for 100 s in order to reduce thermal inhomogeneity. To minimize the friction effect, graphite sheets with a thickness of 0.1 mm were inserted between the specimen and anvils.

The as-deformed microstructure was revealed on the section parallel to the compression axis across the centerline, Samples were prepared by using the conventional methods for the microstructural study. Observation was made with a scanning electron microscope equipped with an EBSD detector.

Table 1: Chemical composition of the AA7020 aluminum alloy used in this research.

Element	Si	Fe	Cu	Mn	Mg	Zn	Ti	Cr	Zr	Al
wt.%	0.31	0.28	0.2	0.34	1.24	4.36	0.001	0.1	0.08	Base

3 Results and discussion

3.1 Microstructural evolution during hot deformation

Fig. 1 (a) shows the microstructure of the AA7020 aluminum alloy before the hot compression test. It can be observed that the initial microstructure is composed of a coarse grain structure with an average grain size of about 250 µm. The grain structure of the samples after hot deformation are shown in Figs. 1 (b) to (d). It can be seen that the microstructures, regardless of the deformation conditions, are composed of deformed grains. Recrystallized grains, to be detected as fine circular ones, are hardly observed. The grain structure and the substructure of the alloy can affect its flow stress during hot deformation. In order to be able to precisely estimate the flow stress of the alloy during deformation, it is important to ensure that the microstructure is recrystallized or elongated after deformation. Indeed, since the alloy is one with high SFE, if the microstructure is not recrystallized, it can be concluded that a substructure exists. In order to make sure, the EBSD map of the sample deformed at 450 °C and strain rate of 0.1 s^{-1}, is shown in Fig. 2.

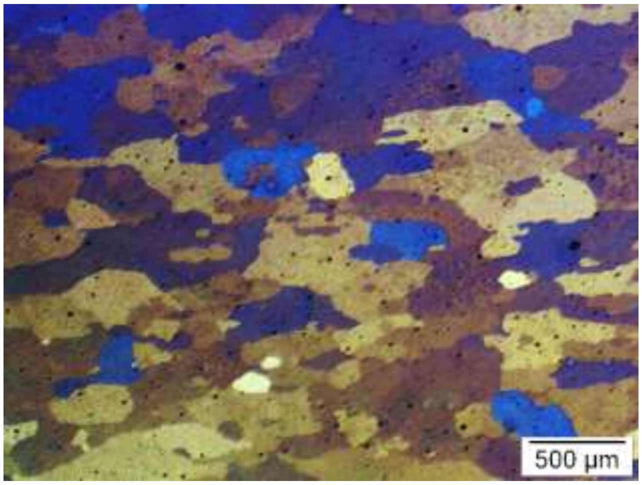

(a)

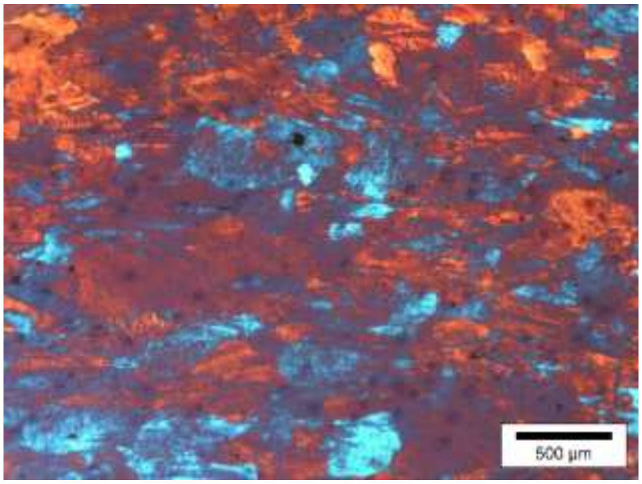

(b)

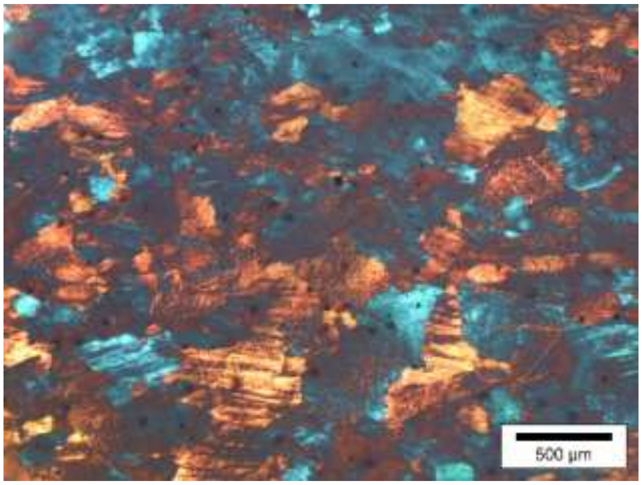

(c)

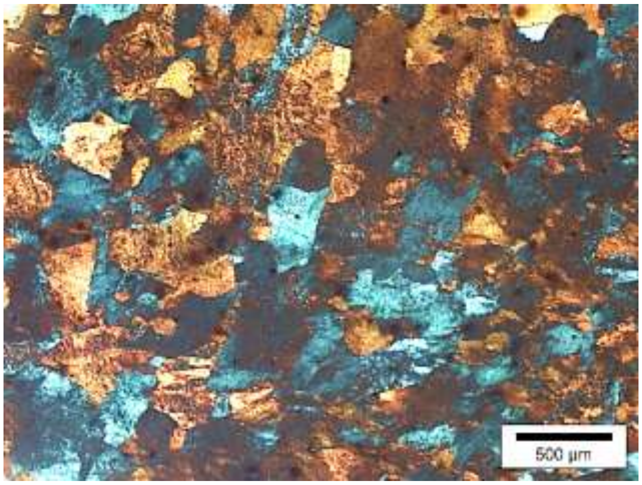

(d)

Fig. 1: (a) Initial microstructure of AA7020 alloy prior to deformation and after deformation at (b) 400 °C and 1 s^{-1}, (c) 450 °C and 1 s^{-1} and (d) 500 °C and 1 s^{-1}.

Substructure of the sample deformed at 450 °C and a strain rate of 0.1 s^{-1} is shown in Fig. 2. It can be seen that subgrains with low angle grain boundaries (white lines) are distributed throughout the as-deformed microstructure. The fact that the substructure is formed in this alloy during hot deformation in addition that the microstructure was not recrystallized indicates that the flow stress of this material during hot deformation may be precisely predicted using substructure based model.

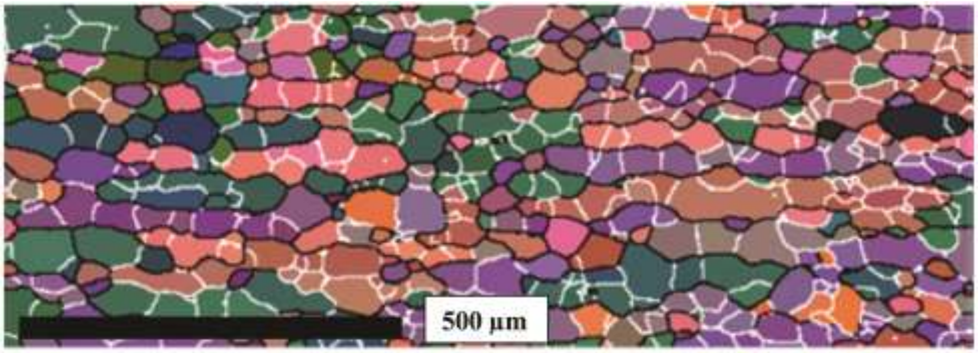

Fig. 2: The substructure formed in a sample deformed at 450 °C and a strain rate of 0.1 s^{-1}.

3.2 Flow stress of the material during hot deformation

The true stress–true strain curves obtained from the hot compression of the AA7020 aluminum alloy are shown in Fig. 3. As can be clearly seen, flow stress rises rapidly at the initial stage of deformation and then stays at a constant level after the maximum stress, called saturated stress, is reached. Retention of flow stress at a constant level with increasing plastic strain at almost all the deformation conditions applied indicates dynamic flow softening as the main restoration mechanism. In principle, hot deformation entails competitive phenomena of dynamic work softening and work hardening. At the commencement of high-temperature deformation, dislocation density intensely increases due to strain hardening, leading to quick increases in flow stress. As deformation continues, a restoration phenomenon, such as DRV and/or DRX is triggered to take place, which can balance or partially compensate the effect of work hardening, and finally the true stress remains unchanged with rising true strain.

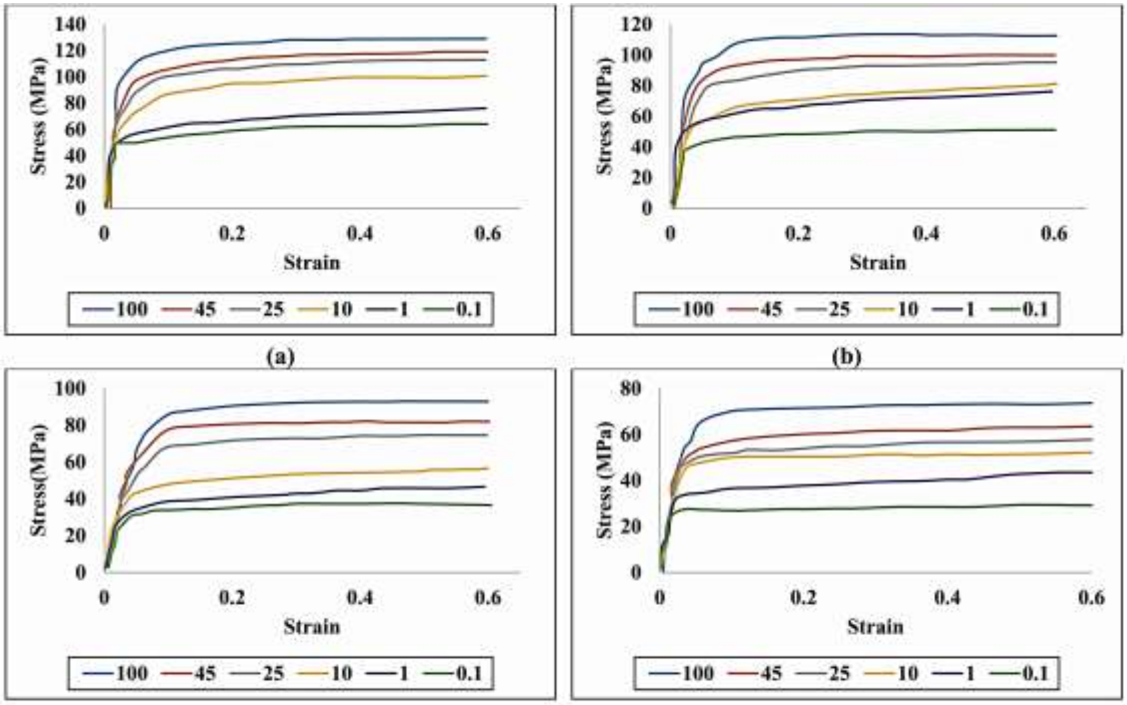

(c) (d)

Fig. 3: Stress-strain curves of AA7020 at different strain rates and temperatures of (a) 350, (b) 400, (c) 450 and (d) 500 ^{o}C.

In the case of the AA7020 aluminum alloy with high SFE, the increase in flow stress at the initial stage of deformation can be attributed to the increases in dislocation density, which consequently, leads to cell formation, dislocation tangles and finally the formation of subgrain boundaries as a combined result of strain hardening and dynamic recovery (DRV). The values of flow stress and steady-state stress decrease with increasing temperature and decreasing strain rate applied during the hot compression tests. When strain rate is fixed, with increasing deformation temperature, dynamic softening becomes more obvious, leading to the decreases in true stress. As temperature increases, DRV accelerates and the critical strain for the development of a subgrain structure decreases. Moreover, at a higher temperature, the mobility of grain boundaries increases, which results in an upturn in the kinetics of DRV. On the other hand, at a fixed temperature, as strain rate increases, the flow stress increases, which indicates that this high SFE material is quite sensitive to strain rate. As a matter of fact, if deformation occurs in a short period of time, there is insufficient time for dislocation movements and then the rate of DRV decreases and flow stress increases.

It is well known that dislocation generation and movements during deformation lead to strain hardening, whereas dislocation rearrangement and further annihilation are caused by restoration through DRV, possibly followed by continuous dynamic recrystallization (CDRX). However, at the deformation conditions applied in this research, i.e., high temperatures and low strain rates, the initially formed low angle subgrain boundaries get enough required activation energy and time to transform themselves into high angle grain boundaries, which consequently yields new strain-free grains. For this Al alloy with high SFE, subgrain structures with low angle grain boundaries are formed during deformation due to proficient DRV and they gradually develop into high angle grain boundaries at larger strains.

The transformation of low angle subgrain boundaries into high angle grain boundaries usually takes place through homogeneous increases in misorientation of low angle boundaries at a relatively high deformation temperature by progressive lattice rotation near grain boundaries or by the development of micro-shear bands (MSBs) at higher plastic strains (Humphreys and Hatherly, 2012). These mechanisms have been detected during thermomechanical processing of materials other than Al alloys (Gourdet and Montheillet, 2000; Lin et al., 2013), such as 304-type austenitic stainless steel (Yanushkevich et al., 2015) and microduplex stainless steel (Tsuzaki et al., 1996). For Al alloys, however, CDRX takes place by progressive accumulation of dislocations into low angle subgrain boundaries, which subsequently intensifies their misorientations and in the end high angle grain boundaries are formed when misorientation angles reach a critical value (15°).

3.3 Substructure-based constitutive equations

During thermomechanical processing of alloys, two key phenomena, i.e., work hardening and work softening, concurrently take place due to the generation and annihilation of dislocations, respectively. The dominant phenomenon and related mechanism dictate the flow stress variation trend. The occurrence of work hardening results in an increase in dislocation density. On the other hand, work softening is a thermally activated phenomenon, causing decreases in overall system energy via two major restoration mechanisms, namely DRV and DRX. DRV, which is much more overriding in high SFE materials than DRX, such as the AA7020 alloy in this investigation, fulfills the mentioned task by dislocation rearrangement and further cell formation in the substructure. The resultant dislocation density distribution depends on both work hardening and work softening rates. The rate of dislocation density (ρ) variation with strain ε can be expressed as (Jonas et al., 2009; Mostafaei and Kazeminezhad, 2012):

$$\frac{d\rho}{d\varepsilon} = h - r\rho \qquad (1)$$

where *h* is the work hardening rate and *r* is the dynamic softening rate at any specified deformation conditions. By integrating Eq. 1, ρ can be expressed as a function of *h*, *r* and *ε,* considering C_1 as the integration constant:

$$\rho = \frac{h}{r} - \frac{C_1}{r}\exp(-r\varepsilon) \qquad (2)$$

Assigning the value of ρ_0 to the dislocation density just before high-temperature deformation ($\varepsilon = 0$), the definite integration constant can be determined and Eq. 2 can be rewritten as:

$$\rho = \rho_0 \exp(-r\varepsilon) + \frac{h}{r}\left[1 - exp(-r\varepsilon)\right] \qquad (3)$$

According to the correlation between dislocation density and stress as expressed in Eq. 4, the dependence of high-temperature flow stress σ and yield stress σ_0 on ρ can be defined by Eqs. 5 and 6 with a slight modification (Nes et al., 2002):

$$\sigma = \alpha G b\sqrt{\rho} \qquad (4)$$

$$\rho = \left(\frac{\sigma}{\alpha G b}\right)^2 \qquad (5)$$

$$\sigma_0 = \alpha G b\sqrt{\rho_0} \qquad (6)$$

In the abovementioned mathematical descriptions, α is a constant value typically of the order of 0.5, and *G* and *b* are the physical terms for describing shear elastic modulus and Burger’s vector.

During the hot compression tests, the flow stress of this high SFE Al alloy approaches a constant value, named DRV saturated stress σ_{RV}, after a certain amount of deformation. By considering Eqs. 3 and 4, Eq. 7 for saturated stress is written:

$$\sigma_{RV} = \alpha G b \sqrt{\frac{h}{r}} \qquad (7)$$

By re-ordering and substituting of the stress and dislocation density terms in Eqs. 4 to 7, the flow stress of a material with DRV dominant deformation behavior can be expressed as:

$$\sigma^2 = \sigma_{RV}^2 + (\sigma_0^2 - \sigma_{RV}^2)\exp(-r\varepsilon) \qquad (8)$$

Using Eq. 8, the kinetics of DRV for the AA7020 aluminum alloy during thermomechanical processing can be identified. For this, three key parameters present in Eq. 8, i.e., saturated stress, yield stress and dynamic softening rate, must be recognized. By differentiating Eq. 8, Eq. 9 is obtained:

$$\frac{d\sigma}{d\varepsilon} = 0.5 \times \left[\sigma_{RV}^2 + (\sigma_0^2 - \sigma_{RV}^2)\exp(-r\varepsilon)\right]^{-0.5} \times (\sigma_0^2 - \sigma_{RV}^2)\exp(-r\varepsilon)\, r \qquad (9)$$

Considering Eq. 8, the term $\frac{\sigma^2 - \sigma_0^2}{\sigma_{RV}^2 - \sigma_0^2}$ can be replaced by the exponential term of $exp(-r\varepsilon)$ and Eq. 9 can be rewritten as Eq. 10:

$$\frac{d\sigma}{d\varepsilon} = 0.5r\,\left(\frac{\sigma_{RV}^2 - \sigma^2}{\sigma}\right) \qquad (10)$$

From now on, the work hardening rate will be represented by the term θ based on Eq. 11 and hence, Eq. 10 can be used in the form of Eq. 12:

$$\theta = \frac{d\sigma}{d\varepsilon} \qquad (11)$$

$$\sigma\frac{d\sigma}{d\varepsilon} = 0.5r\,(\sigma_{RV}^2 - \sigma^2) \qquad (12)$$

By plotting θ against σ^2 at all the hot working temperatures of 350, 400, 450 and 500 °C (Fig. 4) and by using the mentioned terms of Eq. 12, the terms of $-0.5r$ and $0.5r\sigma_{RV}^2$ can be calculated as the slope and the intercept of the graph, respectively.

Consequently, by simple calculations, *r* and σ_{RV} values at all deformation temperatures and strain rates can be determined. Tables 2 and 3 list the dynamic softening rate and saturated stress values of the AA7020 alloy, respectively.

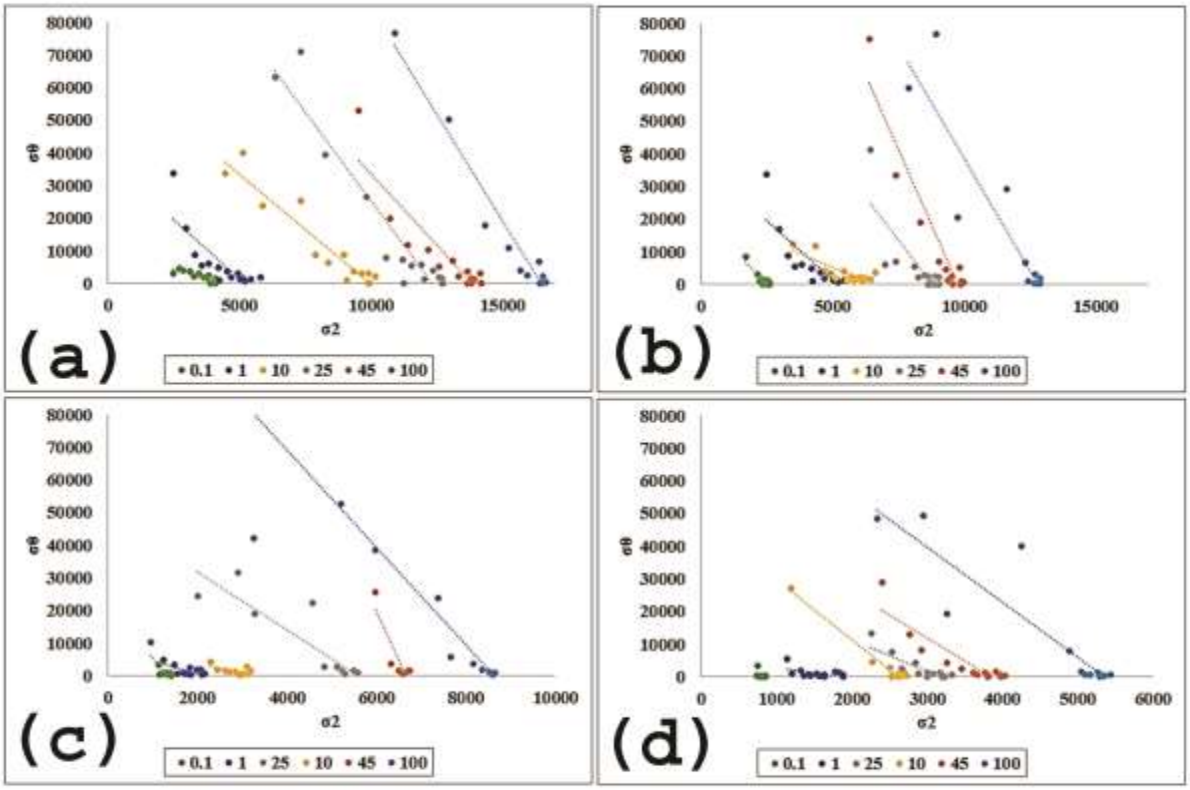

Fig. 4: $\theta\sigma - \sigma^2$ curves for AA7020 at different strain rates and temperatures of (a) 350, (b) 400, (c) 450 and (d) 500 ^{o}C.

After that, the plastic strain where the softening phenomenon begins to get activated after initial work hardening can be found by identifying the point, at which the strain-stress curve shows a tendency to become plateaued. This is representative of dislocation re-arrangement and cell formation at DRV steps after the initial formation of dislocation tangles through work hardening. The resulting plastic strains in all deformation conditions can be found in Table 4. As the values of *r* and σ_{RV} at different deformation conditions were calculated at the previous step, the yield stress σ_0 could be estimated using regression analysis of the experimental stress-strain curves (Table 5).

Increasing strain rate may lead to two key effects of higher deformation heating and enhanced work hardening due to stress increase, which act reciprocally but on the opposite side of each other's and the dominance of them will be changed at different temperatures regarding activating mechanisms. It can be assumed that at 350^{o}C, the process of thermally-activated cross-slip and climb of dislocations become more active at low and high strain rates with respect to mild strain rates, at which, a rise in strain rate from 25 to 45 s^{-1} increases the dislocation generation rate, drives the formation of less recovered substructure and so effectively reduces the time to reach dislocation density in the steady-state region of DRV. On the other side at relatively higher temperatures of 450^{o}C, the thermal circumstance is good enough for having a relatively steady recovery rate and increasing strain rate from low 25s^{-1} to 45s^{-1} facilitate the restoration phenomena by creating more potent zones for DRV. But, by more increasing of strain rate to extreme values of 100 s^{-1}at very high temperature persuasive conditions leads to both higher dislocation mobility and generations that impose some localized strain localization and flow instability that give rises to decreasing r by consuming energy in negative route. In the end, both the number and the size of dislocation cells increase simultaneously with the increase of strain rate, which is conducive to balancing the effects of softening and work hardening with different extent of affection on parameter of r.

In order to model and describe the flow stress-strain curves of the AA7020 alloy with DRV as the main restoration mechanism, the computed r, σ_0 and σ_{RV} values for all the deformation conditions were filled in Eq. 8. The main advantage of using such an approach and formulation in modeling the flow stress-strain curves of the alloy is considering both the effects of work hardening and DRV. It can be clearly seen that the predicted flow curves are in good agreement with the experimental data extracted from the hot compression tests, particularly for low stress levels where the major mechanism is DRV. However, at relatively high stress levels and at final deformation steps, non-conformity is seen between the predicted and experimental stress values, which can be attributed to the following two factors. The first factor is the friction on both ends of buckled cylindrical specimens. The second factor is the diminishing role of DRV at relatively high strains and increasing misorientaions between adjacent subgrains, which finally gives rise to gradual activation of CDRX. Moreover, it can be recognized that the predicted maximum flow stress is almost equal to the saturated stress.

As another proof of the efficiency and accuracy of the proposed substructure-based model, since the curves derived from the constitutive equation of DRV are in good agreement with the results from the hot compressions tests, the key softening mechanism for the AA7020 alloy is DRV. Thus, the proposed model is accurate and applicable for such a high SFE Al alloy. For evaluating the accuracy and efficiency of the analytical dislocation-based model, the cross-validation of the experimental data versus the predicted data is shown in Fig. 5.

Table 2: Values of *r* at all deformation conditions.

T (^{0}C)	Strain rate (s^{-1})					
	0.1	1	10	25	45	100
350	4.9	14.5	13.5	20.5	17.4	26.18
400	16.4	14.6	6.68	20.9	36.7	27.5
450	30.2	29.4	27.5	17.9	58.8	29.9
500	7.02	5.9	36.5	19.7	28.2	29.6

Table 3: Values of σ_{RV} at all deformation conditions.

T (^{0}C)	Strain rate (s^{-1})					
	0.1	1	10	25	45	100

350	65.6	72.1	99.7	114.3	117.7	128.3
400	50.5	71.8	81.1	93.7	98.7	113.2
450	36.8	58.3	73.9	74.2	81.6	92.9
500	29.7	43.5	51.2	56.2	62	69.8

Table 5: Values of σ_0 at all deformation conditions.

T (^{0}C)	Strain rate (s^{-1})					
	0.1	1	10	25	45	100
350	34.5	51.5	52.5	56.6	68.4	91.6
400	26.6	51.3	42.7	46.4	57.4	80.9
450	19.4	41.6	38.9	36.7	47.4	66.4
500	15.6	31.1	26.9	27.8	36.0	49.9

Table 4: Values of strain at which dynamic recovery initiates at all deformation conditions.

T (^{0}C)	Strain rate (s^{-1})					
	0.1	1	10	25	45	100
350	0.122	0.075	0.098	0.085	0.075	0.135
400	0.102	0.77	0.085	0.087	0.08	0.14
450	0.113	0.65	0.079	0.078	0.077	0.111
500	0.093	0.6	0.09	0.76	0.065	0.125

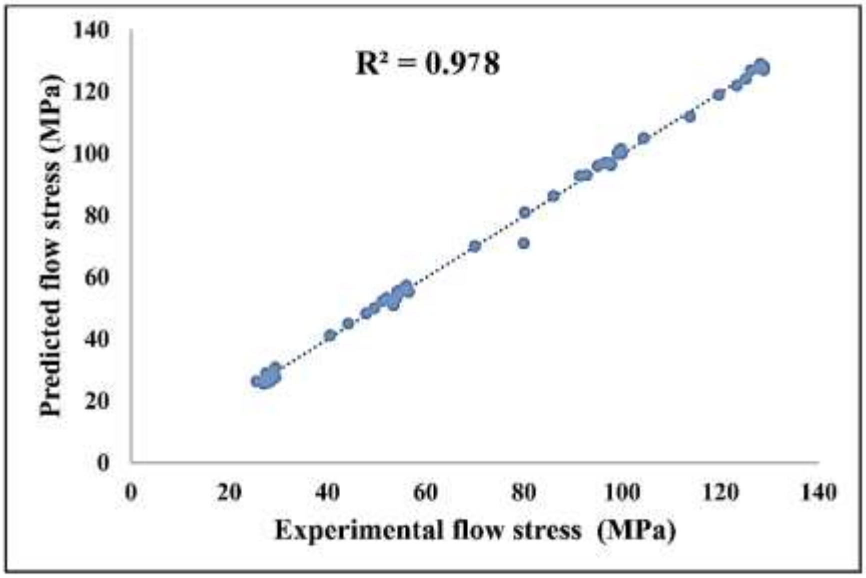

Fig. 5: Relationship between the experimental and analytically predicted flow stresses. The solid line and the markers show the experimental and predicted results, respectively

3.4 True stress estimation using radial basis functions

Mesh-free methods using radial basis functions (RBFs) have been proven to be an advantageous problem-solving approach, especially in tackling complex geometry and high dimensional problems. The only required input for such methods is the data points distributed in the domain instead of being concerned with the connectivity of the nodes (such as FEM). Mesh-free methods using RBFs were first introduced by Hardy (Hardy, 1971) in 1971, taking advantage of the multiquadric (MQ) function as the operating radial basis function. After the initial development of the model, Franke (Franke, 1982) examined various methods to solve two-dimensional scattered-data interpolation problems and concluded that Hardy's approach was the most efficient for modeling. It was also demonstrated that the interpolation matrix of many RBFs are invertible, which can be considered as the major benefit of these functions.

RBFs tend to approximate multivariable (also called multivariate) functions by using a linear combination of terms based on a single univariate function that is called the radial basis function. In the fundamental concept of the mesh-free approximation methods and according to Eq. 13, a multi-dimensional dataset can be transformed into a real integer using the continuous radial basis function ϕ:

$$\phi: \mathbb{R}^m \to \mathbb{R} \qquad (13)$$

A radial basis function in $\mathbb{R}$ space is a function of the form $\phi(||\mathbf{x} - \mathbf{x}_j||)$ where $\mathbf{x}$, $\mathbf{x}_j \in \mathbb{R}^m$ and $||.||$ denote the Euclidean distance between $\mathbf{x}$ and $\mathbf{x}_j$ s vectors.

If one chooses N points $\{\mathbf{x}_j\}_{j=1}^{N}$ in $\mathbb{R}^m$, by subsequent use of the interpolation function of s($\mathbf{x}$) = $\sum_{j=1}^{N} \phi(||\mathbf{x} - \mathbf{x}_j||)\, j \in \mathbb{R}$, a one-dimensional output is yielded.

Different kinds of radial basis functions (ϕ) that have been utilized in function estimation and data interpolations are listed in Table 6.

Table 6: Definitions of some types of RBFs

Name	Definition
Gaussian (GA)	$\phi(\mathrm{r}) = \mathrm{e}^{\frac{-\mathrm{r}^2}{\mu^2}}$
Multiquadric (MQ)	$\phi(\mathrm{r}) = \sqrt{\mathrm{r}^2 + \mu^2}$
Inverse Multiquadric (IMQ)	$\phi(\mathrm{r}) = (\mathrm{r}^2 + \mu^2)^{-\frac{1}{2}}$
Inverse Quadric (IQ)	$\phi(\mathrm{r}) = (\mathrm{r}^2 + \mu^2)^{-1}$
Cubic	$\phi(\mathrm{r}) = \lvert\mathrm{r}\rvert^3$

The term $r = (||\mathbf{x} - \mathbf{x}_j||)$ symbolizes the distance between x and the j–th nodal point $\mathbf{x}_j$ and the μ signifies the shape parameter. Parameter μ is a parameter for controlling the shape of functions which affects the convergence rate and prevents the model from localization. This category of mesh-free methods are usually applied to approximate functions or data which are only known at a finite number of points (or too difficult to evaluate) so that evaluation of the approximating function can take place efficiently. The methods usually work in n dimensional Euclidean space which is called R_n fitted with the

Euclidean norm ‖·‖. There are m points in this space at which the function to be approximated is known and can be written as $\mathbf{x}_1$, $\mathbf{x}_2$… $\mathbf{x}_m$. These points are usually assumed to be all different from each other; otherwise the problem will become singular when interpolation is used. Both *n* and *m* are positive integers. In modeling thermomechanical processing, every x_i is the deformation condition that influences the material response at a given deformation condition, i.e., temperature, strain rate and strain. Any given sets of hot defamation parameters can be transformed to a radialized value using functions of $f(\mathbf{x}_1)$, $f(\mathbf{x}_2)$….$f(\mathbf{x}_\mathbf{m})$ based on the abovementioned concept that comes from the function $f: R^m \rightarrow R$. The established function may be entirely unidentified, excluding data at *m* points or too difficult or time-consuming to evaluate. The schematic paradigm of the RBF approach for the estimation of function values at a specific domain with some known values is illustrated in Fig. 6.

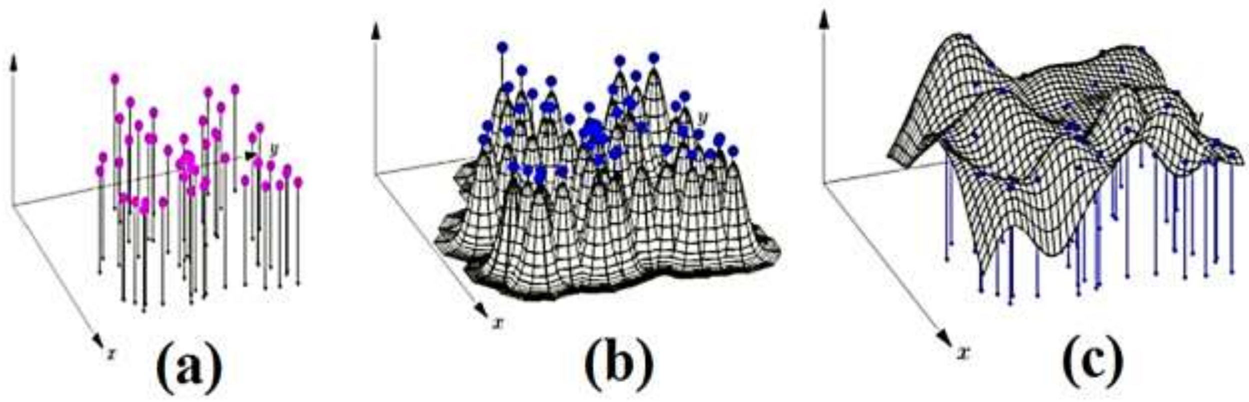

Fig. 6: Schematic demonstration of different steps of the RBF approach: (a) scattered data within a 2-D region (b) radial basis functions, here ‘rotated’ Gaussian RBF and (c) linear combination of the basis function that fits all the data.

To approximate flow stress at any deformation condition, true stress at an arbitrary point x (which represents a set of temperature - strain rate - strain) can be written as a linear combination of *m* basis functions listed in Table 6, as can be seen in Eq. 14:

$$\sigma(\mathbf{x}) \approx S(\mathbf{x}) = \sum_{j=1}^{m} c_j \phi\left(||\mathbf{x} - \mathbf{x}_j||\right) \qquad (14)$$

where m is the number of data points, $\{c_j\}_{j=1}^{m}$ are the set of coefficients to be determined. In this research, the Gaussian radial basis function with μ=0.5 was employed in the estimation model to predict flow stress from a set of deformation parameters for the AA7020 Al alloy (Fig. 7). It should be noted that the expansion coefficients c_j are determined by the interpolation conditions $\mathrm{s}(\mathbf{x}_i) = f_i$.

From a mathematical point of view, it can be expressed by solving a linear system of Eq. 15:

$$Ac = f \tag{15}$$

where the entries of the matrix A, c and f are defined according to Eqs. 16 to 18:

$$A_{i,j} = \phi(||\mathbf{x}_i - \mathbf{x}_j||)_{1\leq i\leq m, 1\leq j\leq m} \tag{16}$$

$$f = [f_1 \cdots f_m]^T \tag{17}$$

$$\boldsymbol{c} = [c_1 \cdots c_m]^T \tag{18}$$

The matrix notation of Eq. 15 can be defined as Eq. 19:

$$\begin{bmatrix} \phi(||\mathbf{x}_1 - \mathbf{x}_1||) & \phi(||\mathbf{x}_1 - \mathrm{x}_2||) & \cdots & \phi(||\mathbf{x}_1 - \mathbf{x}_m|| \\ \phi(||\mathbf{x}_2 - \mathbf{x}_1||) & \phi(||\mathbf{x}_2 - \mathbf{x}_2||) & \cdots & \phi(||\mathbf{x}_2 - \mathbf{x}_m||) \\ \vdots & \cdots & \ddots & \vdots \\ \phi(||\mathbf{x}_\mathrm{m} - \mathbf{x}_1||) & \phi(||\mathbf{x}_\mathrm{m} - \mathbf{x}_2||) & \cdots & \phi(||\mathbf{x}_\mathrm{m} - \mathrm{x}_m||) \end{bmatrix} \begin{bmatrix} c_1 \\ c_2 \\ \vdots \\ c_m \end{bmatrix} = \begin{bmatrix} f_1 \\ f_2 \\ \vdots \\ f_m \end{bmatrix} \tag{19}$$

It is worthy of note that the estimation of $f\ (x)$ is unique if the matrix A is nonsingular. After solving the abovementioned linear system, the c vector was determined and the interpolation estimation function could be expressed according to Eq. 14 for describing flow stress as a function of strain, strain rate and temperature. The scatter map of the predicted and measured flow stresses is displayed in Fig 8.

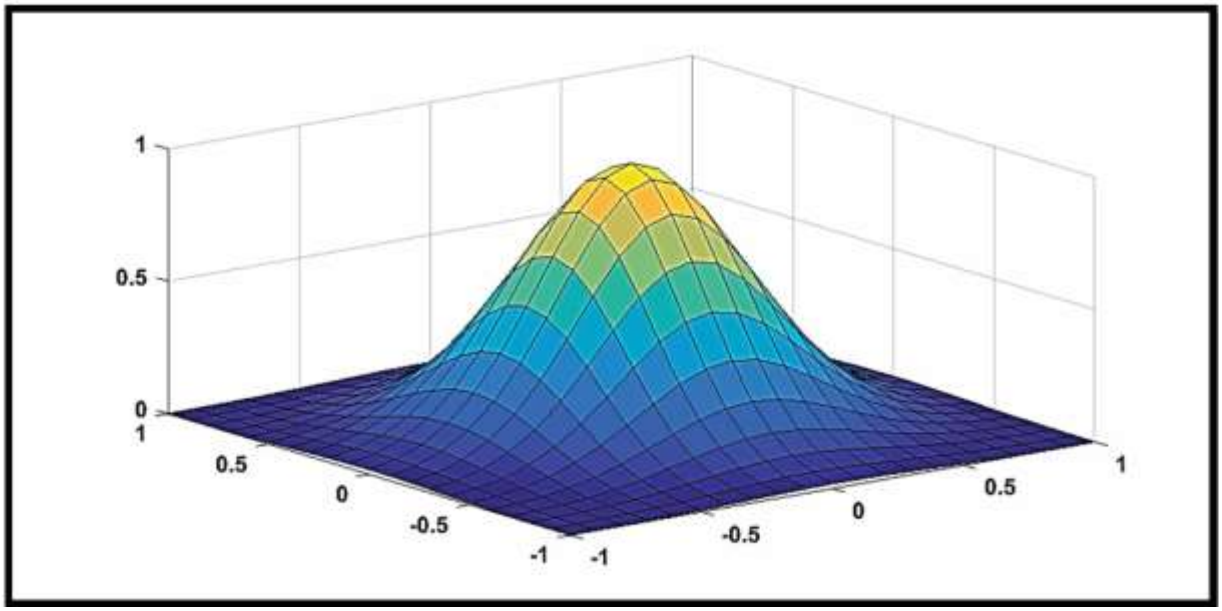

Fig. 7: Gaussian radial basis function with μ=0.5 used in this research.

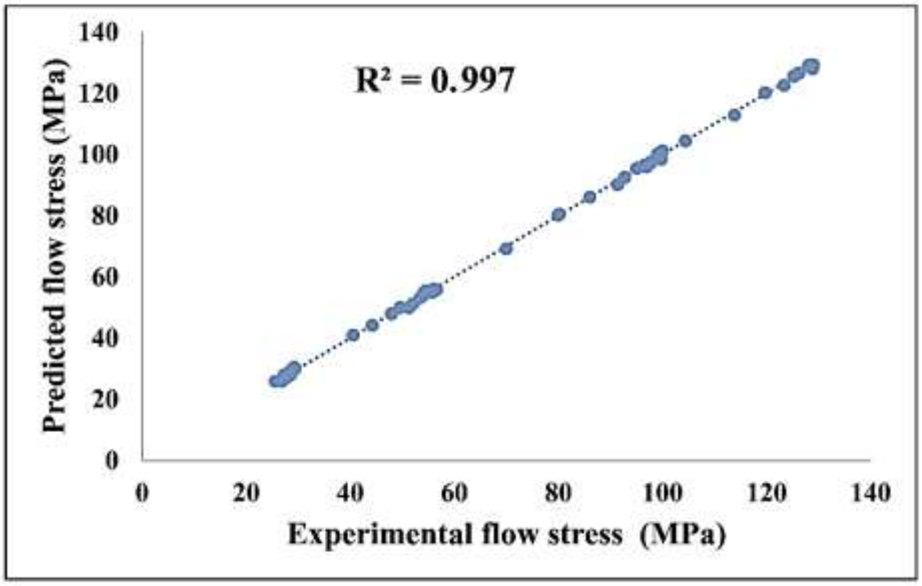

Fig. 8: Relationship between the experimental and RBF predicted flow stresses. The solid line and the markers show the experimental and predicted results, respectively.

Radial basis function (RBF) methods can provide excellent interpolating operator for high dimensional data sets of poorly distributed data points (scarce and unevenly distributed points). For any finite data set in any Euclidean space, one can construct an interpolation of the data by using RBFs, even if the data points are unevenly and sporadically distributed in a high dimensional Euclidean space. Implementing RBF methods requires choosing which basis functions to use, and many basis functions are defined by a shape parameter which must also be chosen. The choices made have a tremendous impact on the accuracy of the results and the numerical stability of the method used. Among radial basis functions methods, Gaussian RBF methods, are one of the most referenced in literature for solving wing weight fitting problems. For our data set, Gaussian RBF methods presented the most desirable results. Many RBF methods contain a free shape parameter that plays an important role for the accuracy of the method. Different shape parameters correspond to different approximations resulting from RBF interpolation. Finding the shape parameter that will produce the most accurate approximation. Optimal shape parameter values are found experimentally and these values are written for interpolating problems. Theoretically, RBF methods are most accurate when the shape parameter is small. However, the use of small shape parameters results in system matrices that are very poorly conditioned. The by now very established fact that in RBF methods is that we cannot have both good accuracy and good conditioning at the same is known as the uncertainty principle. About the case that why one should use a "relatively small" shape parameter. The reason is to offer a little bit extra smoothness, as a too large shape parameter won't work. It should be pointed out that generally the choice of the optimal shape parameter in RBFs is still an open problem. Determination of suitable shape parameter is extracted experimentally for GA- RBFs used in this study, which is 0.5.

3.5 Comparison between the proposed models

To evaluate the predictive proficiency of the developed RBF approach, comparisons between the experimental and predicted flow stresses by RBF, as well as substructure-based constitutive model were made. Fig. 9 shows the predicted and experimental high-temperature stress-strain curves at all the testing conditions. Noticeably, the true stresses predicted by the RBF approximation method are closer to the experimentally measured values than those calculated by using the dislocation-based constitutive model.

During deformation at high strain rates and low temperatures, the substructure-based constitutive equation could not correctly model the flow stress, while the RBF method could predict the flow stress precisely. According to the strain-stress variation in the predicted curves derived from the constitutive and RBF models, it could be deduced that the dynamic softening phenomenon as a result of DRV was dominant at all temperatures and strain rates.

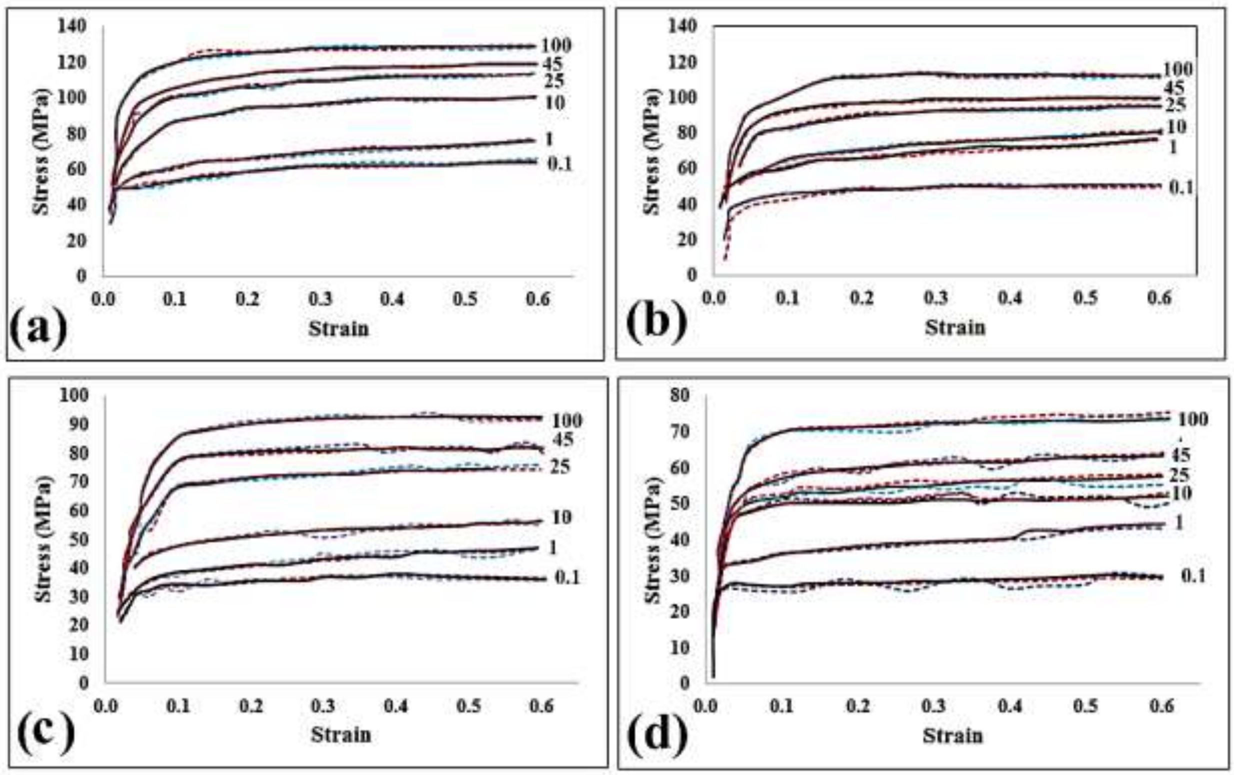

Fig. 9: Comparisons between predicted and experimental stress-strain curves of AA7020 at different strain rates and temperatures of (a) 350, (b) 400, (c) 450 and (d) 500 ^{o}C. (Solid black, dotted blue and dotted red represent experimental, constitutive and RBF predicted results, respectively).

In the application of the constitutive model, the relative error between the predicted and experimental data could be caused by the overestimation of the work hardening phenomenon. As a result, the predicted flow stresses curves from the constitutive model appeared to be higher than the experimental ones. In comparison with the substructure-based constitutive model, the RBF model could accurately describe the high-temperature deformation behavior of this Al alloy and did not involve complex physical mechanisms. This can be inferred from the cross-validation graphs of the predicted and experimental flow stresses shown in Fig. 6 and 8. It is obvious that the predictive capability of the RBF model is higher than that of the constitutive model. In order to further compare the predictive capabilities of the RBF and constitutive models, the correction coefficient R^2 and RMSE values between the measured and predicted true stresses are listed in Table 7. It can be seen that the correction coefficient R^2 values of the constitutive and RBF models are 0.978 and 0.997, respectively, which indicates that the predicted and experimental data are in excellent agreement with each other. In addition, the RMSE value of the RBF model is 2.213, which is much smaller than that of the constitutive model. This confirms that the prediction efficiency and accuracy of the RBF model are superior to those of the constitutive model. In other words, the mesh-free approach using the RBF estimation model can more exactly describe the hot deformation characteristics of the studied aluminum alloy.

Table 7: Statistical criteria for comparing the performance of the RBF and constitutive models.

Approach	R^2	*RMSE*
Constitutive model	0.978	3.056
RBF	0.997	2.213

4 Conclusions

In this research, the hot deformation characteristics of the AA7020 aluminum alloy were investigated by using two modeling approaches. The results obtained from hot compression tests clearly indicated that the developed subgrain substructure due to DRV was influenced by two major deformation parameters, i.e., temperature and strain rate, and subsequent CDRX occurred from the subgrain structure. Flow stress decreased with increasing deformation temperature and decreasing strain rate. By making use of the true stress-strain curves, the radial basis function (RBF) model was developed for assessing the hot deformation behavior of the aluminum alloy. It was demonstrated by using the statistical criteria that the proposed RBF model could correctly and truthfully predict the flow stress-strain curves of the alloy at the all deformation conditions. Compared to the substructure-based constitutive model, the RBF method showed outstanding predictive potential and could be implemented for describing the thermomechanical behavior of the AA7020 aluminum alloy.

5 References

Oliveira, A., De Barros, M., Cardoso, K., Travessa, D., 2004. The effect of RRA on the strength and SCC resistance on AA7050 and AA7150 aluminium alloys. Materials Science and Engineering: A 379, 321-326.

Deng, Y., Yin, Z., Huang, J., 2011. Hot deformation behavior and microstructural evolution of homogenized 7050 aluminum alloy during compression at elevated temperature. Materials Science and Engineering: A 528, 1780-1786.

Jin, N., Zhang, H., Han, Y., Wu, W., Chen, J., 2009. Hot deformation behavior of 7150 aluminum alloy during compression at elevated temperature. Materials Characterization 60, 530-536.

Humphreys, F.J., Hatherly, M., 2012. Recrystallization and related annealing phenomena. Elsevier.

Holm, E.A., Miodownik, M.A., Rollett, A.D., 2003. On abnormal subgrain growth and the origin of recrystallization nuclei. Acta Materialia 51, 2701-2716.

Liu, S., You, J., Zhang, X., Deng, Y., Yuan, Y., 2010. Influence of cooling rate after homogenization on the flow behavior of aluminum alloy 7050 under hot compression. Materials Science and Engineering: A 527, 1200-1205.

Mirzadeh, H., Parsa, M., 2014. Hot deformation and dynamic recrystallization of NiTi intermetallic compound. Journal of Alloys and Compounds 614, 56-59.

Shalbafi, M., Roumina, R., Mahmudi, R., 2017. Hot deformation of the extruded Mg–10Li–1Zn alloy: Constitutive analysis and processing maps. Journal of Alloys and Compounds 696, 1269-1277.

Wen, D.-X., Lin, Y., Chen, J., Chen, X.-M., Zhang, J.-L., Liang, Y.-J., Li, L.-T., 2015. Work-hardening behaviors of typical solution-treated and aged Ni-based superalloys during hot deformation. Journal of Alloys and Compounds 618, 372-379.

Haghdadi, N., Martin, D., Hodgson, P., 2016. Physically-based constitutive modelling of hot deformation behavior in a LDX 2101 duplex stainless steel. Materials & Design 106, 420-427.

Zouari, M., Bozzolo, N., Loge, R.E., 2016. Mean field modelling of dynamic and post-dynamic recrystallization during hot deformation of Inconel 718 in the absence of δ phase particles. Materials Science and Engineering: A 655, 408-424.

Huang, K., Logé, R., 2017. Microstructure and flow stress evolution during hot deformation of 304L austenitic stainless steel in variable thermomechanical conditions. Materials Science and Engineering: A 10, 600-610.

Ashtiani, H.R., Shahsavari, P., 2016. A comparative study on the phenomenological and artificial neural network models to predict hot deformation behavior of AlCuMgPb alloy. Journal of Alloys and Compounds 687, 263-273.

Yao, C., Wang, B., Yi, D., Ding, X., 2014. Artificial neural network modelling to predict hot deformation behaviour of as HIPed FGH4169 superalloy. Materials Science and Technology 30, 1170-1176.

Zhao, J., Ding, H., Zhao, W., Huang, M., Wei, D., Jiang, Z., 2014. Modelling of the hot deformation behaviour of a titanium alloy using constitutive equations and artificial neural network. Computational Materials Science 92, 47-56.

Fasshauer, G.E., 2007. Meshfree Approximation Methods with Matlab. World Scientific Publishing Company, Incorporated.

Buhmann, M.D., 2003. Radial Basis Functions: Theory and Implementations. Cambridge University Press.

Eivani, A., Zhou, J., Duszczyk, J., 2014. Numerical modeling of subgrain growth of hot extruded Al–4.5 Zn–1Mg alloy in the presence of nanosized dispersoids. Computational Materials Science 86, 9-16.

Wendland, H., 2004. Scattered Data Approximation. Cambridge University Press

Lin, Y., Li, L.-T., Xia, Y.-C., Jiang, Y.-Q., 2013. Hot deformation and processing map of a typical Al–Zn–Mg–Cu alloy. Journal of Alloys and Compounds 550, 438-445.

Raj, R., 1981. Development of a processing map for use in warm-forming and hot-forming processes. Metallurgical and Materials Transactions A 12, 1089-1097.

Srinivasan, N., Prasad, Y., Rao, P.R., 2008. Hot deformation behaviour of Mg–3Al alloy—A study using processing map. Materials Science and Engineering: A 476, 146-156.

Wang, S., Hou, L., Luo, J., Zhang, J., Zhuang, L., 2015. Characterization of hot workability in AA 7050 aluminum alloy using activation energy and 3-D processing map. Journal of Materials Processing Technology 225, 110-121.

Blum, W., Zhu, Q., Merkel, R., McQueen, H., 1996. Geometric dynamic recrystallization in hot torsion of Al-5Mg-0.6 Mn (AA5083). Materials Science and Engineering: A 205, 23-30.

Hausselt, J., Blum, W., 1976. Dynamic recovery during and after steady state deformation of Al-11wt% Zn. Acta Metallurgica 24, 1027-1039.

Sakai, T., Miura, H., Goloborodko, A., Sitdikov, O., 2009. Continuous dynamic recrystallization during the transient severe deformation of aluminum alloy 7475. Acta Materialia 57, 153-162.

Eivani, A.R., Zhou, J., Duszczyk, J., 2012. A new approach to incorporating the effect of nano-sized dispersoids on recrystallization inhibition into Monte Carlo simulation. Computational Materials Science 54, 370-377.

Radhakrishnan, B., Sarma, G., Zacharia, T., 1998. Modeling the kinetics and microstructural evolution during static recrystallization—Monte Carlo simulation of recrystallization. Acta Materialia 46, 4415-4433.

Shen, X.-m., Guan, X.-j., Zhang, J.-x., Liu, Y.-t., Ma, X.-f., Zhao, X.-m., 2007. Coupling of FEM with Monte Carlo for simulating recrystallization in cold rolling pure aluminum sheet. Chinese Journal of Nonferrous Metals 17, 124.

Eivani, A., Zhou, J., Duszczyk, J., 2014. Numerical modeling of subgrain growth of hot extruded Al–4.5 Zn–1Mg alloy in the presence of nanosized dispersoids. Computational Materials Science 86, 9-16.

Raabe, D., Becker, R.C., 2000. Coupling of a crystal plasticity finite-element model with a probabilistic cellular automaton for simulating primary static recrystallization in aluminium. Modelling and Simulation in Materials Science and Engineering 8, 445.

Salehi, M.S., Serajzadeh, S., 2012. Simulation of static recrystallization in non-isothermal annealing using a coupled cellular automata and finite element model. Computational Materials Science 53, 145-152.

Gourdet, S., Montheillet, F., 2000. An experimental study of the recrystallization mechanism during hot deformation of aluminium. Materials Science and Engineering: A 283, 274-288.

Yanushkevich, Z., Belyakov, A., Kaibyshev, R., 2015. Microstructural evolution of a 304-type austenitic stainless steel during rolling at temperatures of 773–1273K. Acta Materialia 82, 244-254.

Tsuzaki, K., Huang, X., Maki, T., 1996. Mechanism of dynamic continuous recrystallization during superplastic deformation in a microduplex stainless steel. Acta Materialia 44, 4491-4499.

Jonas, J.J., Quelennec, X., Jiang, L., Martin, É., 2009. The Avrami kinetics of dynamic recrystallization. Acta Materialia 57, 2748-2756.

Mostafaei, M., Kazeminezhad, M., 2012. A novel approach to find the kinetics of dynamic recovery based on hot flow curves. Materials Science and Engineering: A 544, 88-91.

Nes, E., Marthinsen, K., Brechet, Y., 2002. On the mechanisms of dynamic recovery. Scripta Materialia 47, 607-611.

Hardy, R.L., 1971. Multiquadric equations of topography and other irregular surfaces. Journal of geophysical research 76, 1905-1915.

Franke, R., 1982. Scattered data interpolation: tests of some methods. Mathematics of computation 38, 181-200.